

https://dspace.org/

Solgel synthesis and photoluminescent properties of metal oxidemetal oxide coupled nanocomposites

Busisiwe Petunia Mabuea; Robin Edward Kroon; Buyisiwe Mavis Sondezi; Odireleng Ntwaeaborwa

ELSEVIER SCIENCE BV
https://hdl.handle.net/10539/40668
WOS

Downloaded from a DSpace repository. https://dspace.org/

Physica B 675 (2024) 415600

Contents lists available at ScienceDirect

Physica B: Condensed Matter

journal homepage: www.elsevier.com/locate/physb

Sol-gel synthesis and photoluminescent properties of metal oxide-metal oxide coupled nanocomposites

Busisiwe Petunia Mabuea [a,d,*], Robin Edward Kroon [b], Buyisiwe Mavis Sondezi [a], Odireleng Martin Ntwaeaborwa [c]

[a] Department of Physics, University of Johannesburg, P.O. Box 524, Auckland Park, 2006, South Africa
[b] Department of Physics, University of the Free State, P.O Box 339, Bloemfontein, 9300, South Africa
[c] School of Physics, University of the Witwatersrand, Private Bag 3, Wits, 2050, South Africa
[d] Advanced Materials Engineering, Manufacturing Cluster, Council for Scientific and Industrial Research, P.O. Box 395, Pretoria, 0001, South Africa

ARTICLE INFO

Keywords:
Photoluminescence
Coupling
Metal-oxides
Nanocomposites
Zinc oxide
Tin oxide

ABSTRACT

Tin oxide (SnO_2) and zinc oxide (ZnO) coupled metal-oxide nanocomposites or SnO_2–ZnO were prepared using a sol-gel method. The stretching mode frequencies and crystal structures were examined by using Fourier transform infrared spectroscopy (FTIR) and X-ray diffraction (XRD), respectively. The microscopic analyses by scanning electron microscopy (SEM) and transmission electron microscopy (TEM) showed a flower-like morphology of the nanocomposites. The analysis of surface chemical and electronic states was conducted by X-ray photoelectron spectroscopy (XPS). The band gap energies as confirmed from the ultraviolet–visible spectroscopy (UV–Vis) data were found to be larger than those of the bulk band gaps due to the increase between energy levels associated with smaller particle sizes. The UV (380 nm) and orange (595) photoluminescence (PL) emissions observed from the SnO_2:ZnO nanocomposites were attributed to a combinatorial contribution from radiative transitions in SnO_2 and ZnO components. The proposed mechanisms of these emissions are discussed.

1. Introduction

Coupling two or more materials in nanoscale to form nanocomposites with properties different from those of the individual components that make up the nanocomposites has been a subject of interest for most researchers worldwide [1,2]. Nanocomposites can be chemically and physically manipulated for specific applications since they have been reported to have superior optical, magnetic, chemical, and mechanical properties in comparison with their single components [3]. The coupled semiconductor metal oxides are nanomaterials [4] that are being produced and investigated lately. Metal oxide-based nanocomposites have been reported to have better properties such as enhanced surface area and conductivity and reduced electron-hole recombination rate [5–7], among others. These semiconductor nanocomposites are useful for application in lighting, catalysis, solar energy conversion, gas sensing, biomedical, and pigments [4,8].

Coupling tin oxide (SnO_2) with zinc oxide (ZnO) results in a typical case of semiconducting nanocomposite that is capable of overcoming some of the limitations of single SnO_2 and ZnO components [9]. SnO_2–ZnO composite has been found to achieve efficient charge separation and improved photoluminescence (PL) properties [10] better than those of the individual components. ZnO is a well-known n-type semiconductor with a direct bulk band gap energy of ~3.37 eV and a large exciton binding energy of about 60 meV [11], which is suitable for excitonic recombination for use in UV excitonic lasers, tunable photodetectors, and charge carriers in photovoltaic cells. It is chemically stable, has a broad range of radiation absorption and high electrochemical coupling coefficient [12]. Musa et al. [13] investigated the PL properties of ZnO nanorods with controlled lengths and diameters. Their PL results showed strong ultra-violet (UV) emission at ~395 nm (when the nanorod's length was reduced) and a visible emission at ~580 nm, which they attributed to excitonic recombination and oxygen vacancies in the bandgap, respectively. SnO_2 is also an n-type semiconductor with a bulk energy band gap of ~3.8 eV [14,15], with good electrical and optical properties [9]. The PL studies of nanocrystalline SnO_2 powder for optoelectrical devices by Nehru et al. [16] showed PL emission band with a maximum at ~620 nm, which they also attributed to oxygen defects within the band gap. Coupling SnO_2 with another smaller band

* Corresponding author. Department of Physics, University of Johannesburg, P.O. Box 524, Auckland Park, 2006, South Africa.
E-mail address: bmabuea@csir.co.za (B.P. Mabuea).

https://doi.org/10.1016/j.physb.2023.415600
Received 23 May 2023; Received in revised form 7 October 2023; Accepted 11 December 2023
Available online 20 December 2023
0921-4526/© 2023 Elsevier B.V. All rights reserved.

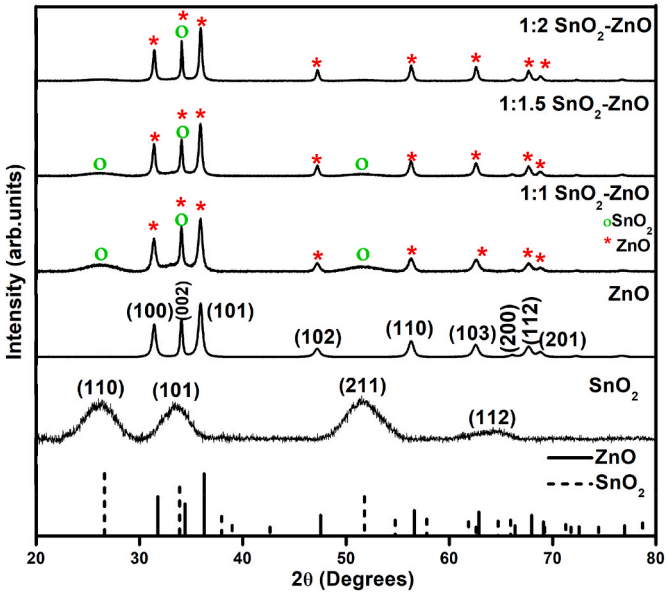


Fig. 1. XRD patterns of SnO_2–ZnO nanocomposites.

gap semiconducting material has been reported to enhance its luminescing properties allowing the charge separation by accumulating electrons and holes in separate particles [17]. Furthermore, SnO_2 is an attractive candidate for application in optoelectrical devices, catalysis, lithium-ion batteries, and solid-state lighting [18].

In this study, we investigated the crystal structure, particle morphology, electronic and elemental composition, optical and luminescent properties of the SnO_2–ZnO nanocomposites with distinct molar ratios of SnO_2 to ZnO.

Several methods such as hydrothermal, co-precipitation, combustion route, calcination process, sol-gel, solvothermal, etc. Have been used to synthesize metal-oxides in powder form [18]. The sol-gel method has advantages such a cost-effectiveness, green energy-saving and it uses smaller amounts of precursor materials. Notwithstanding the fact that SnO_2–ZnO nanocomposites have been reported, in our study we demonstrated how to engineer the band gap by varying the ratio of Zn: Sn, and the utility of the PL spectroscopy data in locating the positions of intrinsic defects within the band gap. The effects of varying the ratios of SnO_2 to ZnO on the fundamental properties of the SnO_2–ZnO nanocomposites are reported. The composites exhibited UV (~380 nm) and orange emission (~595 nm) associated, respectively, with excitonic recombination in the ZnO bandgap and intraband defect states in SnO_2 and ZnO. The objective of the study was to investigate the effect of Sn–Zn coupling with different molar ratios on photoemission of the SnO_2:ZnO nanocomposites. Possible mechanisms of radiative emissions associated with the nanocomposites are discussed. The nanocomposites were evaluated for use in different types of light emitting devices.

2. Experimental

2.1. Materials

Tin (IV) chloride pentahydrate ($SnCl_4{\cdot}5H_2O$), ammonium hydroxide solution (NH_4OH), sodium hydroxide pellets (NaOH), ethanol (CH_3CH_2OH) and zinc acetate dihydrate ($Zn(CH_3COO)_2{\cdot}2H_2O$) were used as starting materials. These were all analytical grades from Sigma-Aldrich Pty. Ltd. with no refinement.

2.2. Preparation of SnO_2

4 g of $SnCl_4{\cdot}5H_2O$ was dissolved in a solution of CH_3CH_2OH (60 ml) and distilled water (20 ml), followed by vigorous continuously stirring for 30 min until a clear solution was formed. NH_4OH (20 ml) was added dropwise to the solution and a white precipitate was formed. The solution was stirred and allowed to age for 24 h. After the aging process, the precipitate was washed then dried overnight in an oven maintained at 200 °C.

2.3. Preparation of ZnO

2 g of $Zn(CH_3COO)_2{\cdot}2H_2O$ was dispersed in distilled water (40 ml) and stirred for 40 min. NaOH pellets (2 g) were dissolved in distilled water, in a separate beaker. The NaOH solution (60 ml) was added dropwise to the zinc acetate solution and aged for 24 h. The ZnO

Table 1
Average crystallite sizes and lattice strains of SnO_2, ZnO and SnO_2–ZnO.

Material	D (nm) (±1) Scherrer's	D (nm) (±1) Williamson-Hall	ε
SnO_2	3	3	0.00160
ZnO	16	21	0.00291
1:1 SnO_2–ZnO	10	16	0.000954
1:1.5 SnO_2–ZnO	13	23	0.00100
1:2 SnO_2–ZnO	17	23	0.000694

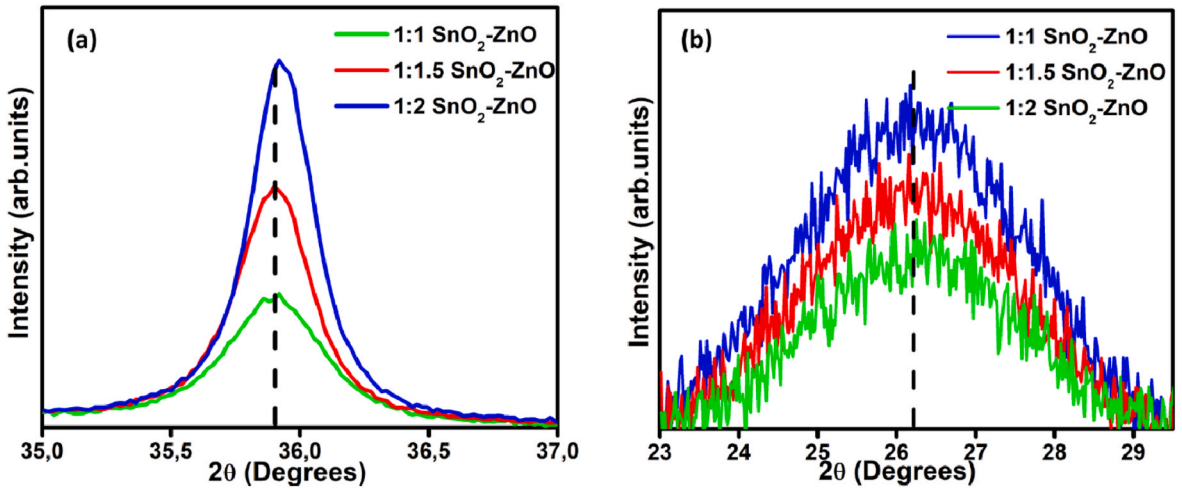


Fig. 2. XRD peaks of SnO_2–ZnO at 35.8° (a) and 26° (b).

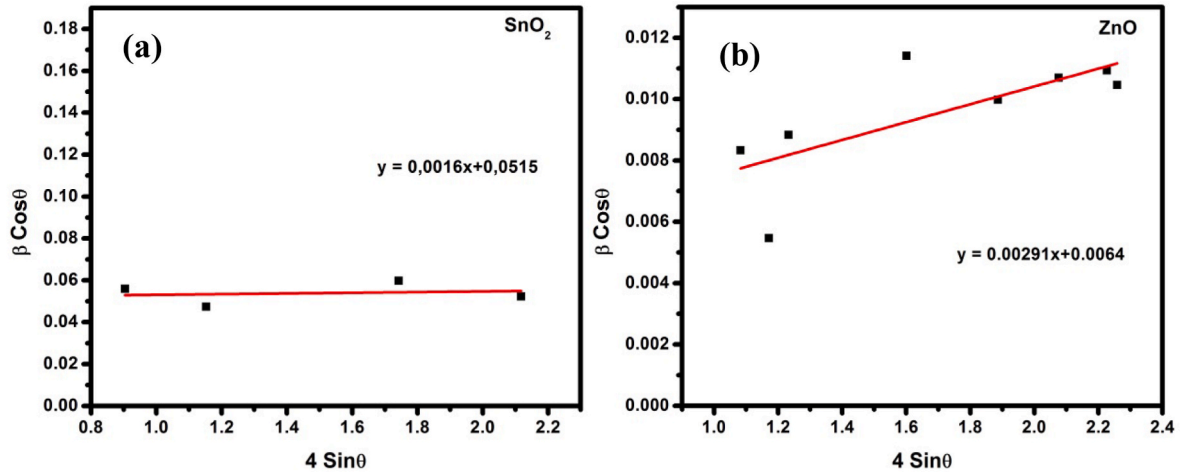


Fig. 3. Williamson-Hall plots of SnO_2 (a) and ZnO (b).

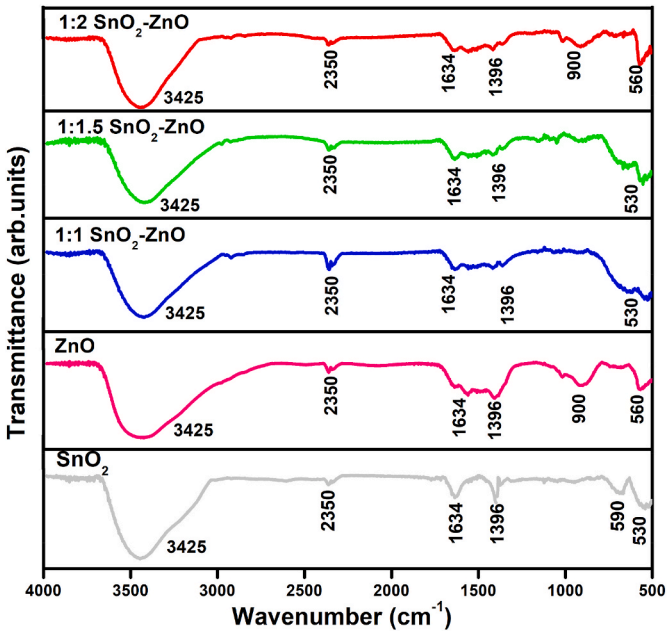


Fig. 4. SnO_2, ZnO and SnO_2–ZnO FTIR spectra.

precipitate was dried overnight in an oven maintained at 60 °C and was subsequently ground using pestle and mortar resulting in a fine powder.

2.4. Preparation of SnO_2–ZnO nanocomposites

0.25 g of the precipitated SnO_2 was dissolved in distilled water (10 ml) and mixed thoroughly by ultrasonication. The dispersion of zinc acetate solution prepared with $Zn(CH_3COO)_2{\cdot}2H_2O$ (2 g), NaOH pellets (2 g) and distilled water (50 ml) was added dropwise to the SnO_2 solution while stirring vigorously. The mixed solution was aged for 24 h, then washed, dried and ground using pestle and mortar.

2.5. Characterization

The crystal structure was analyzed using Bruker D8 Advance X-ray diffraction (XRD). The XRD system was operated with a Cu Kα radiation (λ = 1.5406 Å). The Scherrer's equation was used to calculate the crystallite sizes (D):

$$D = K\lambda/\beta \cos\theta \quad (1)$$

where K is the Scherrer's constant that depends on the shape of the crystallite (0.9 for spherical crystallites), λ is the X-ray wavelength (1.5406 Å), θ is the Bragg's angle and β is the full width at half maximum (FWHM). Since the Scherrer equation only accounts for broadening due to sizes of the crystallites, Williamson-Hall method was used to calculate both the strains (ε) and crystallite sizes caused by lattice dislocation.

$$B\cos\theta = K\lambda/D + 4\varepsilon \sin\theta \quad (2)$$

The chemical bonding and vibrational stretching mode frequencies of the samples were examined using Fourier transform infrared spectroscopy (FTIR) (Thermo Scientific Nicolet 6700). JEOL JSM-7800 F Field emission scanning electron microscope (FESEM) equipped with an Oxford Aztec energy dispersive X-ray spectroscopy (EDS), and JEOL JEM-ARM200F high resolution transmission electron microscope (HRTEM) were used to study morphology, elemental composition and the crystal structure.

Physical electronics PHI VersaProbe XPS microprobe fitted with aluminum X-ray source was used to investigate the electronic and chemical states of the nanocomposites. The binding energy charge was corrected against the carbon-carbon bond at 284.7 eV. The reflectance spectra were measured with a Lambda 950 PerkinElmer UV–visible spectrometer (UV–Vis). The photoluminescence (PL) spectra were recorded using the PL system consisting of the monochromator, photomultiplier tube detector and a 325 nm He–Cd used as excitation source.

3. Results and discussions

3.1. Crystal structure

Fig. 1 shows the XRD spectra of SnO_2, ZnO and SnO_2–ZnO nanocomposites. All the detected peaks were found to be consistent with the standard reference data files: ICDD No. 41–1445 for SnO_2 (tetragonal phase – rutile structure) and ICDD No. 36–1451 for ZnO (hexagonal phase – wurtzite structure). The XRD patterns of SnO_2–ZnO exhibited diffraction peaks associated with both SnO_2 and ZnO, i.e. the diffraction peaks are consistent with those of individual components. The SnO_2 peaks remain broad and less intense due to and insufficient planes of smaller particle sizes and hence incomplete cancelling of incoherent scattering, while the ZnO peaks remain sharp and intense associated with bigger particles that have sufficient unit cells and hence coherent scattering. In the case of the nanocomposite where the ratio of SnO_2 to ZnO was varied, broad peaks along with sharp peaks were observed revealing the small particles associated with SnO_2 (peaks marked with "o" in the patterns of the nanocomposites) and excellent crystallinity associated with bigger ZnO particles (peaks marked with "*" in the

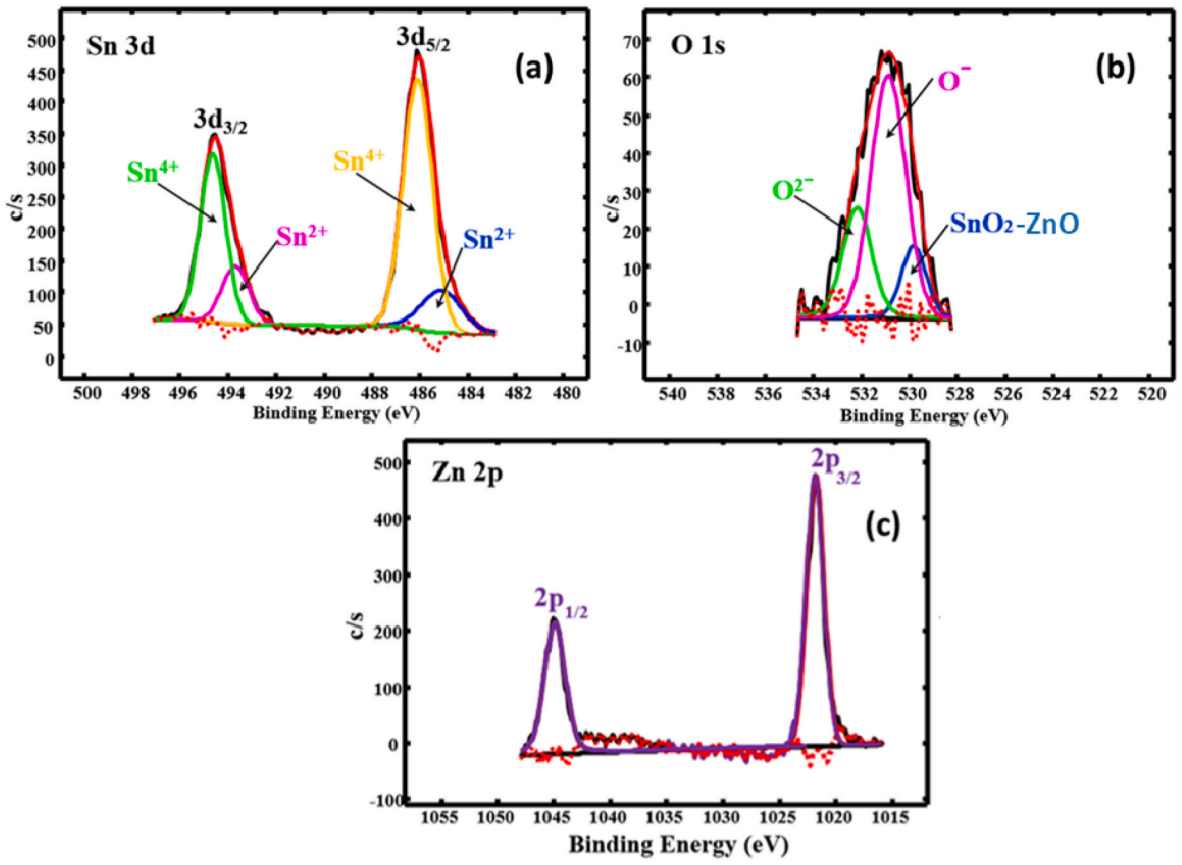


Fig. 5. High-resolution spectra of Sn 2*p* (a), O 1*s* (b), Zn 2*p* (c) and O 1*s* (d).

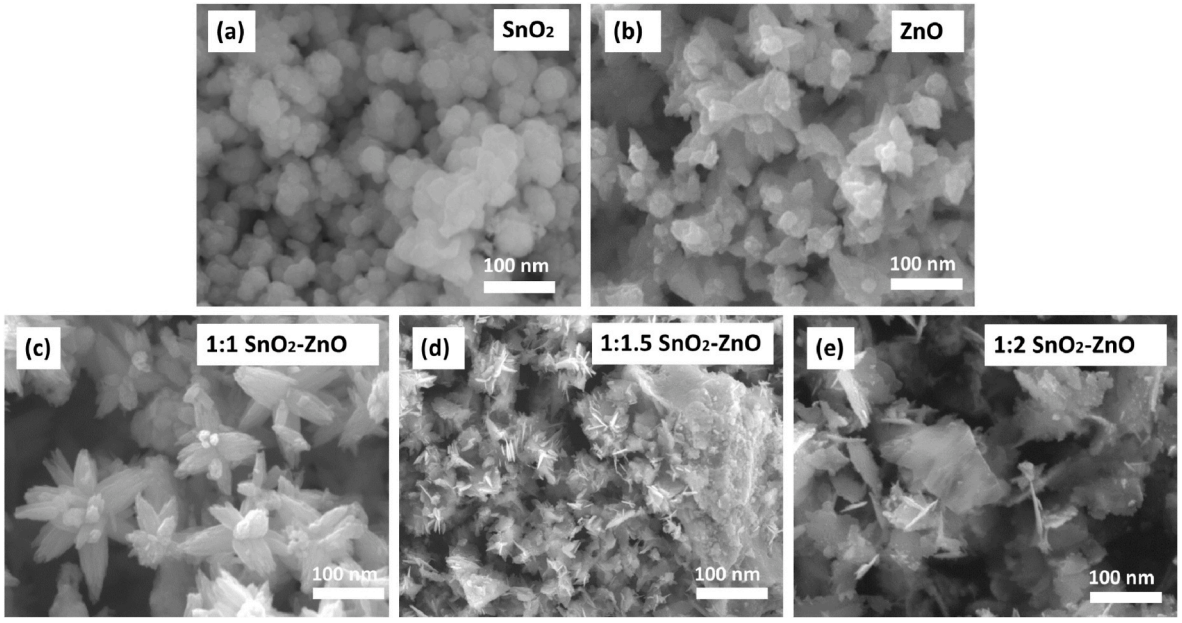


Fig. 6. SEM images of SnO_2 (a), ZnO (b), 1:1 SnO_2–ZnO (c), 1:1.5 SnO_2–ZnO (d) and 1:2 SnO_2–ZnO (e).

patterns of the nanocomposites).

Fig. 2(a) shows the (101) and (110) diffraction peaks for different ratios of SnO_2 to ZnO in the nanocomposites. The ZnO (101) peak shows a slight shift to high values of 2θ degrees with increasing concentration of ZnO. This is due to a decrease in lattice spacing with increasing ZnO content. Furthermore, the crystallinity of the material is improved by an increase in the Zn concentration. There was no peak shifting in the SnO_2 (110) peak as shown in Fig. 2(b), but the peak intensity decreased with increasing Zn concentration.

The average lattice strains and crystallite sizes extracted from the peak width analysis are shown in **Table 1**. The strains (ε) were determined from the slope of the linear fit of the graphs of $\beta cos\theta$ as a function

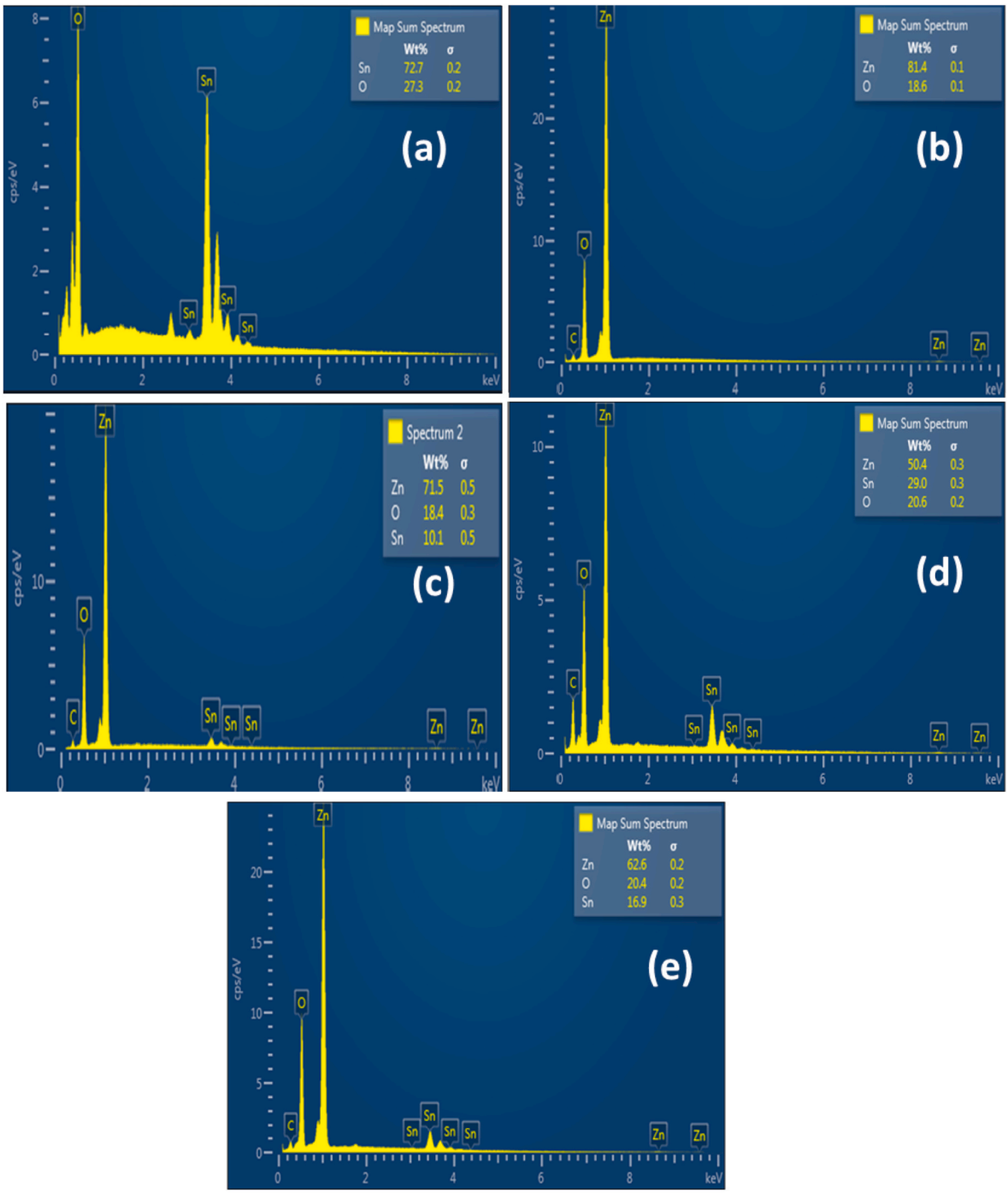


Fig. 7. EDS spectra of SnO_2 (a), ZnO (b), 1:1 SnO_2–ZnO (c), 1:1.5 SnO_2–ZnO (d) and 1:2 SnO_2–ZnO (e).

of $4\sin\theta$ shown in Fig. 3.

The crystallite sizes obtained using Williamson-Hall method are bigger than those obtained by Scherrer's equation. This is because the Scherrer's equation ignore the effect of lattice strain and instrumental broadening factors [19]. The instrumental broadening factor is usually negligibly small.

3.2. Stretching and bending vibrations

Fig. 4 displays the FTIR spectra of SnO_2, ZnO and the SnO_2–ZnO nanocomposites. The Sn–O stretching vibrations were detected at 530 and 590 cm^{-1}, while the stretching mode frequencies for ZnO were detected at 500 cm^{-1}. When comparing the single components with the nanocomposites, they all have peaks at 1396, 1634, 2350 and 3425 cm^{-1} pointing to a successful crystallization of SnO_2–ZnO nanocomposites. The 1396 cm^{-1} peak is ascribed to the bending vibration of H–*O*–H from atmospheric moisture molecules. The bending mode at 1634 cm^{-1} is assigned to the deformation vibration of the *O*–H groups and that at 900 cm^{-1} is assigned to the *C*–H vibrations. The frequency modes at 2350 cm^{-1} and 3425 cm^{-1} are asscribed to the C═O groups and *O*–H vibrations [20], respectively. The increase in ZnO concentration caused the Sn–O and Zn–O vibrations to shift to higher wavenumbers.

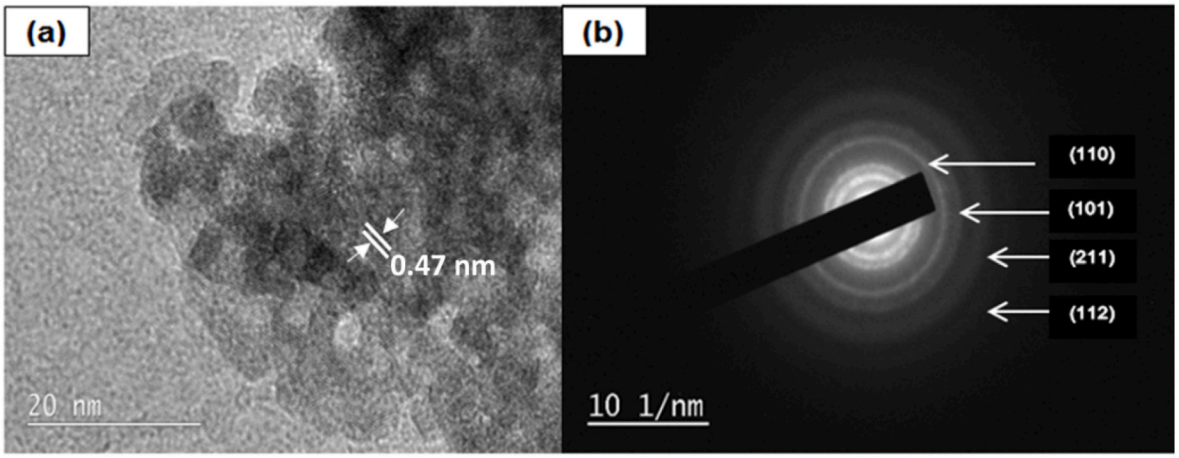


Fig. 8. (a) HR-TEM image, and (b) selected area electron diffraction pattern of SnO_2.

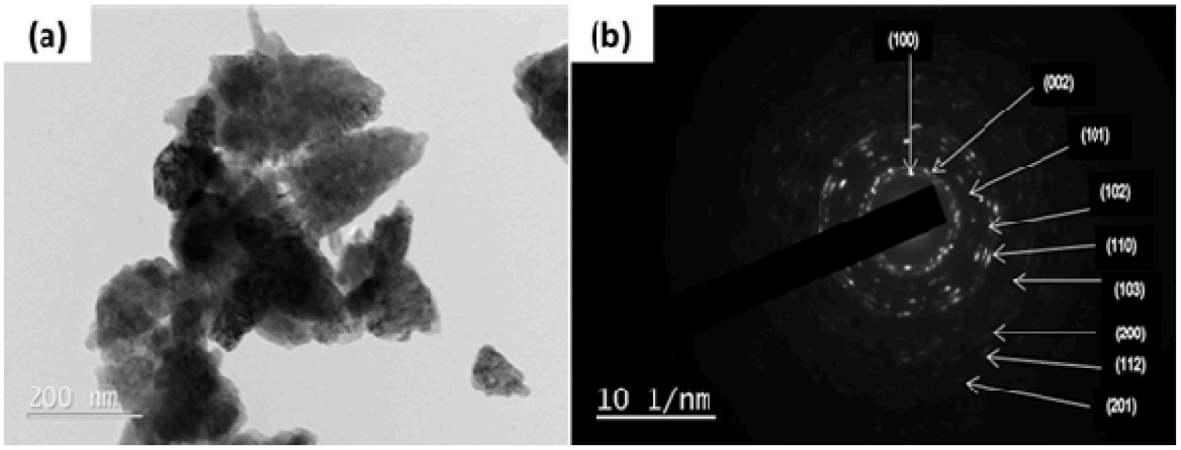


Fig. 9. (a) HR-TEM image and (b) selected area electron diffraction pattern of ZnO.

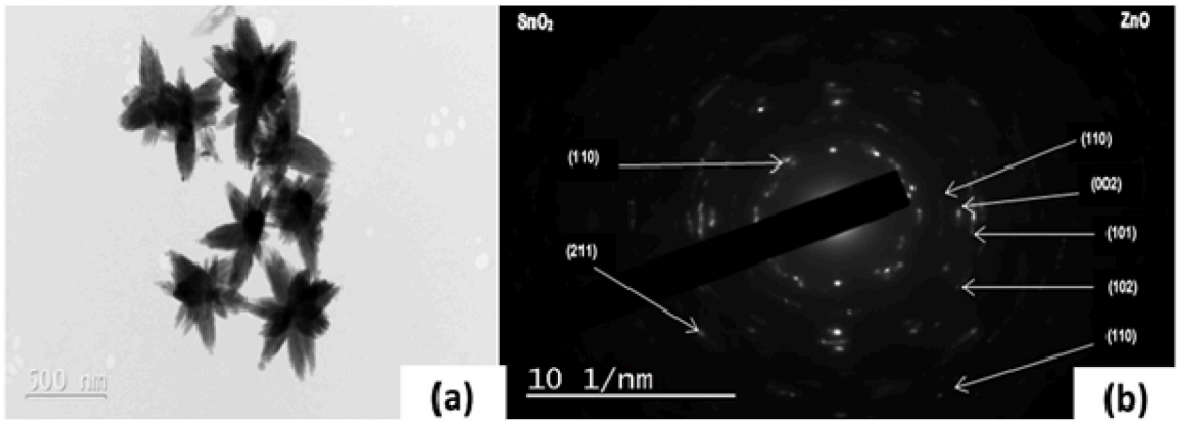


Fig. 10. (a) HR-TEM image and (b) selected area electron diffraction pattern of 1:1 SnO_2–ZnO.

3.3. Surface analysis

The high-resolution XPS spectra of Sn, Zn and O recorded from SnO_2–ZnO are presented in Fig. 5. The Sn 3*d* XPS spectrum in Fig. 5(a) consists of two photoelectron peaks located at the binding energies of 486.5 and 494.5 eV. These peaks are ascribed to Sn $3d_{5/2}$ and Sn $3d_{3/2}$ doublets respectively. The doublets displayed photoelectron lines attributed to the Sn^{4+} (486.5 and 494.5 eV) and Sn^{2+} (485.1 and 493.5 eV) ionic states [21]. Fig. 5(b) show the O 1*s* XPS spectra of SnO_2–ZnO. It consists of three peaks located at 529.8, 530.6 and 532.3 eV. The major peak located at 530.6 eV is due to the chemisorbed oxygen [11]. The shoulder at 529.8 eV is assigned to the O^{2-} lattice ions located in regions with low content of oxygen in the SnO_2–ZnO composite [21], while the shoulder at 532.3 eV is attributed to the loosely bound oxygen with the adjacent Sn^{4+} and Zn^{2+} ions. The photoelectron lines of Zn 2*p* spectra shown in Fig. 5(c) consist of two main peaks centered at 1022.6 and

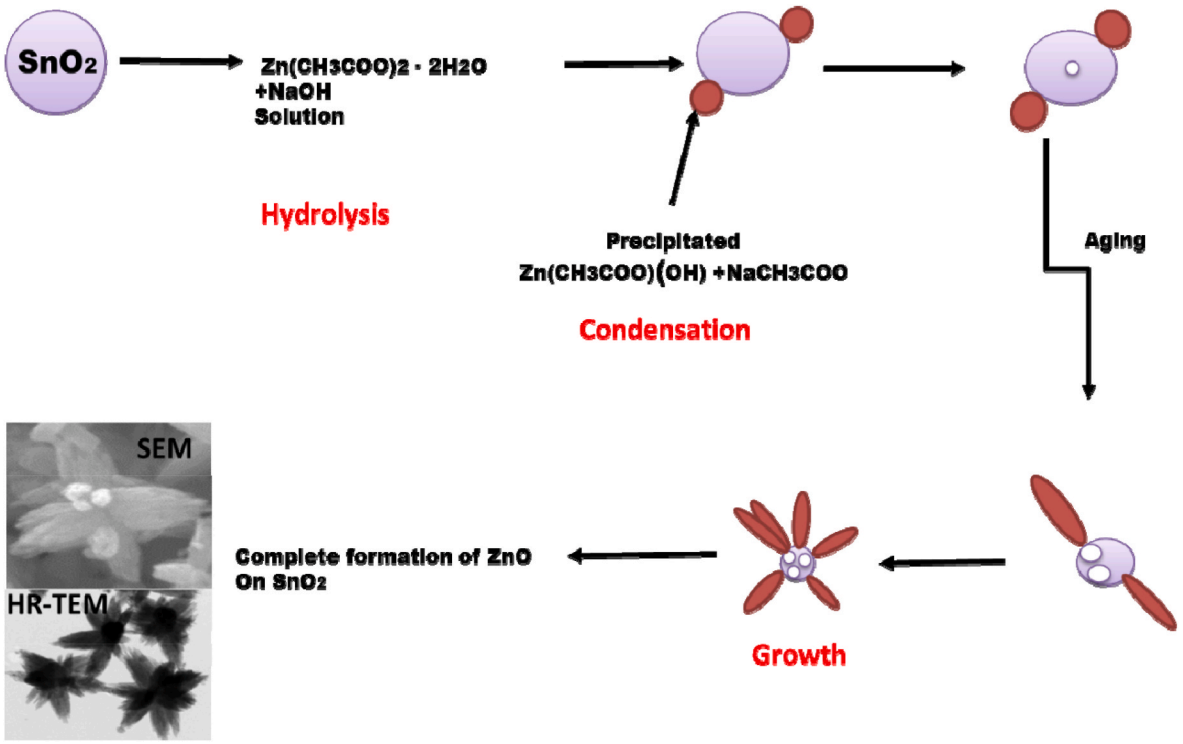


Fig. 11. Growth mechanism of SnO_2–ZnO nanocomposite.

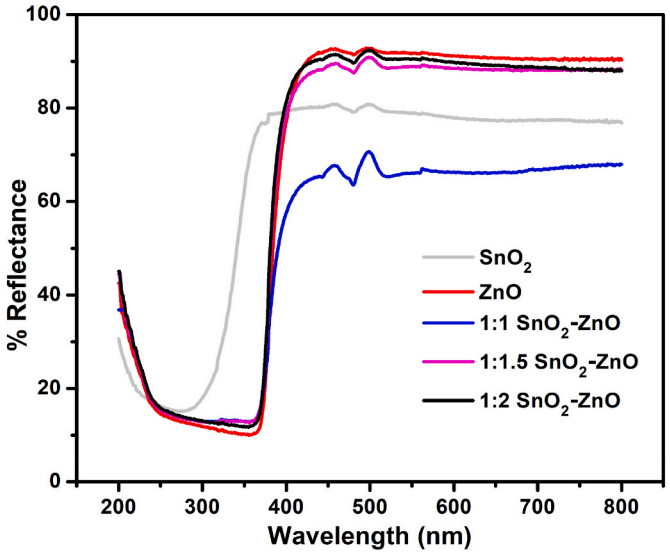


Fig. 12. Reflectance spectra of SnO_2–ZnO nanocomposites.

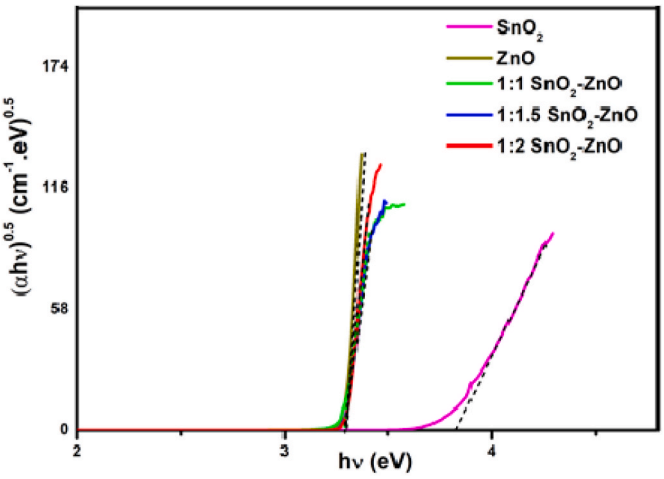


Fig. 13. Tauc plots of SnO_2 (a), ZnO (b), 1:1 SnO_2–ZnO (c), 1:1.5 SnO_2–ZnO (d) and 1:2 SnO_2–ZnO (e) for estimation of band gap energies.

1045.0 eV, which are assigned to $2p_{3/2}$ and $2p_{1/2}$ spin-spin doublets [11, 22].

3.4. Particle morphology and elemental composition analysis

Fig. 6 shows the HR-SEM images of SnO_2, ZnO and SnO_2–ZnO. An agglomeration of smaller, spherically shaped SnO_2 nanoparticles is shown in Fig. 6(a). This agglomeration is ascribed to high number of surface atoms with high surface energy of the nanoparticles. Atoms without complete co-ordinations have vacant co-ordination sites [23]. ZnO (Fig. 6(b)) was made up of flower-like nanoparticles. The SEM does not have the capability to differentiate between the core and shell of a material since the primary electrons only scan across the surface. By comparing the images of all the nanocomposites with distinct molar ratios of SnO_2 to ZnO (Fig. 6(c–e), it is clear from Fig. 6(c) that the ZnO nanoparticles indeed covered the core especially in the 1:1 SnO_2 to ZnO ratio.

The elemental composition is shown in the EDS spectra of Fig. 7. Atomic weight percentage of Sn (72.7 %) and O (27.3 %) in Fig. 7(a) confirms that SnO_2 consists of tin and oxygen elements without any secondary peaks, indicating that the nano-powder was free from impurities. EDS analysis of ZnO (Fig. 7(b)) exhibited peaks of Zn, O and C (from the carbon conductive mounting tape). The high counts per second from the Zn peaks suggest that Zn was distributed evenly on the surface. The atomic weight percentage of Zn is 81.4 % (Zn) and that of O is 18.6 % (O), which is close to the stoichiometric Zn element (80.34 %)

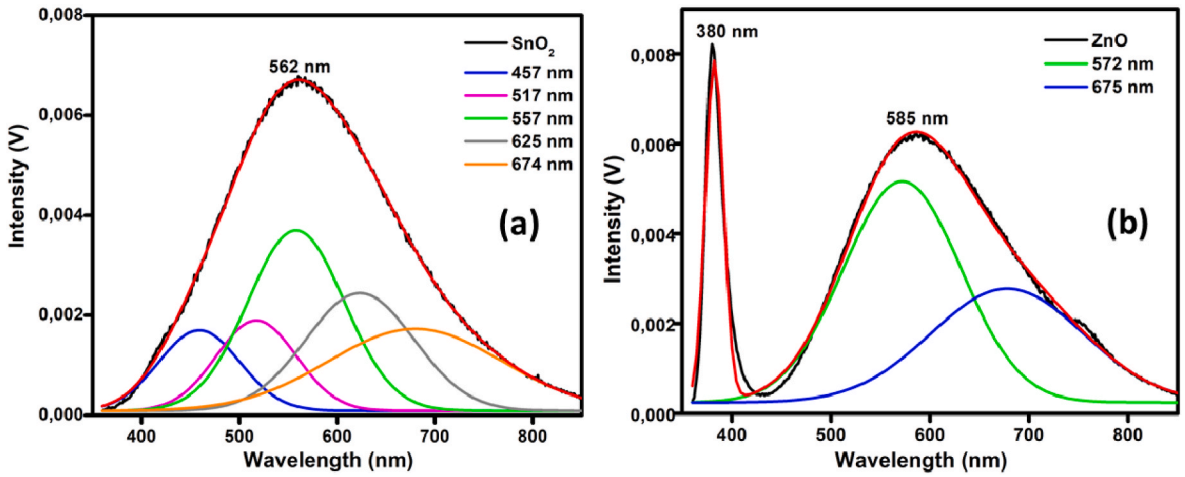


Fig. 14. PL Emission spectra of SnO_2 (a) and ZnO (b).

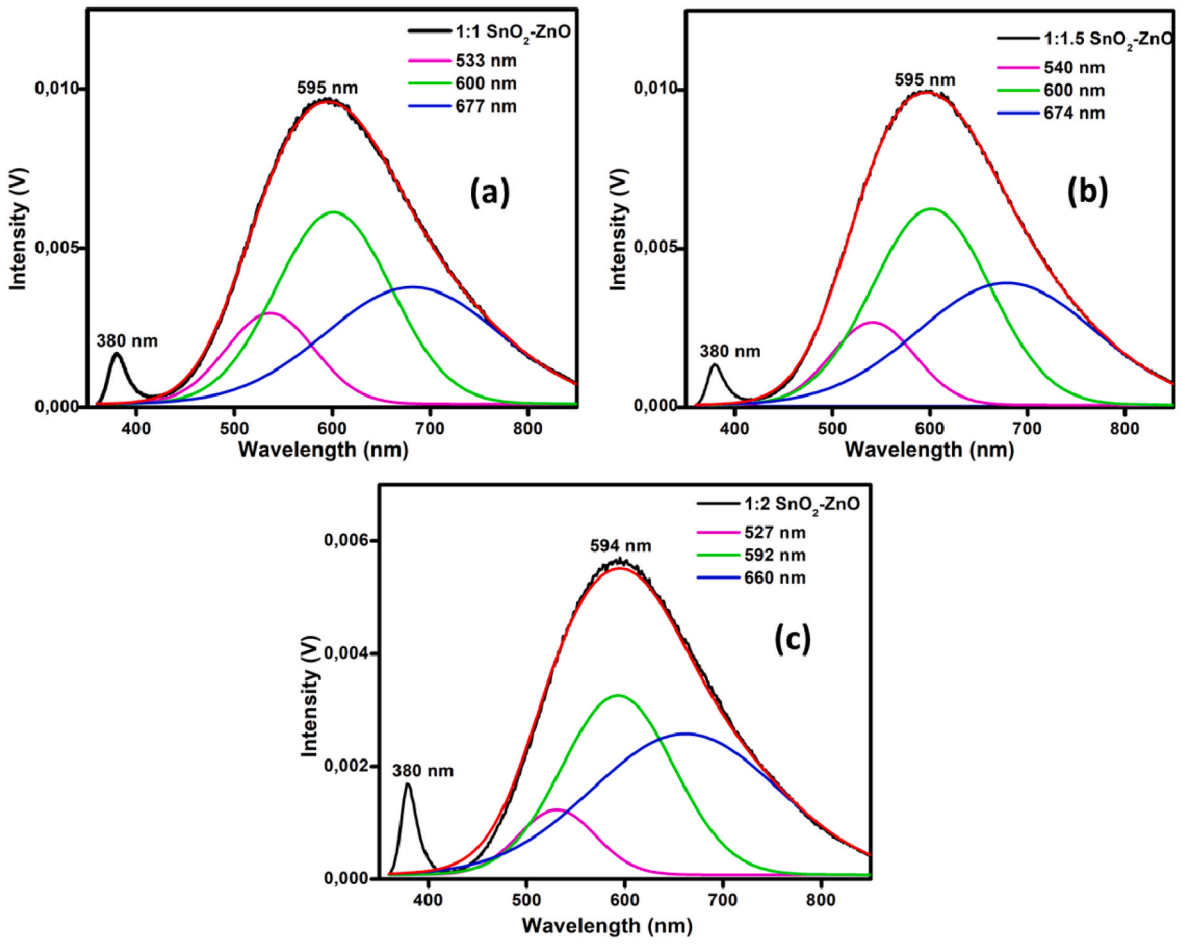


Fig. 15. PL Emission spectra of 1:1 SnO_2–ZnO (a), 1:1.5 SnO_2–ZnO (b), and 1:2 SnO_2–ZnO (c) nanocomposites.

[24]. The EDS elemental composition of the composites, Fig. 7(c–e), also confirmed all the elements present in our samples.

The HR-TEM images in Fig. 8 show morphology and the selected area electron diffraction pattern (SAED) of SnO_2, ZnO and SnO_2–ZnO. Fig. 8 (a) shows spherical morphology of SnO_2 with conspicuous lattice fringes. Consistent with the HRSEM data, the high surface area of the nanoparticles results in particle agglomeration. The SAED pattern in Fig. 8(b) shows a continuous ring of a large number of nanoparticles that precisely match the X-ray diffraction peaks in Fig. 1.

Fig. 9 shows that ZnO powder was composed of chunk of irregularly shaped particles that were agglomerated together. The SAED image shows a ring pattern made up of bright spots. This pattern is due to the diffraction from a single crystal pointing to the formation of ordered crystalline materials. Furthermore, the SAED pattern determines the growth orientation of the ZnO nanoparticles. These patterns are consistent with the X-ray diffraction data, confirming a successful crystallization of ZnO nanoparticles.

The SnO_2–ZnO nanocomposite (Fig. 10) are made up of flower-like

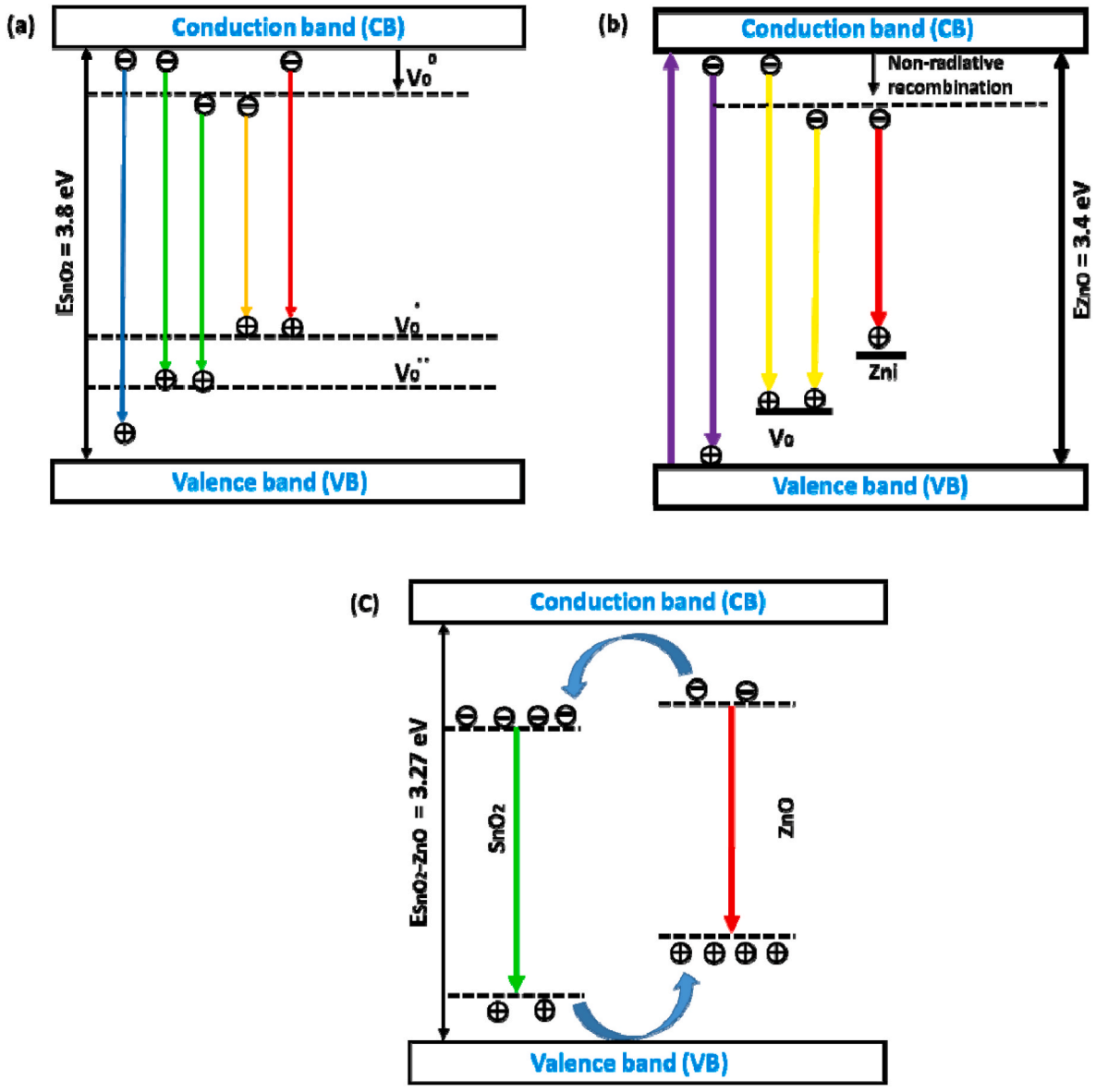


Fig. 16. PL mechanisms of SnO_2 (a), ZnO (b) and SnO_2–ZnO (c).

nanoparticles, consistent with the HRSEM result in Fig. 6. It has been confirmed from the XRD data that the SnO_2 particles are smaller than the ZnO particles; this is also observed in the SAED pattern which shows electron diffraction spots from both SnO_2 and ZnO. The dark area is the core, and the relative bright area is the shell. The darker area indicates that the core absorbed or scattered electrons, while the brighter areas indicates that the shell transmitted electrons.

Fig. 11 shows the proposed formation of ZnO coated SnO_2 synthesized by the sol-gel method that includes three main reactions, namely hydrolysis, condensation, and nucleation and growth. Zinc acetate dihydrate and sodium hydroxide underwent hydrolysis, i.e., they readily reacted with the surrounding water molecules. Condensation took place and a precipitate was formed, as shown by smaller spherical molecules on the SnO_2. These smaller molecules started to arrange themselves and grew slowly due to the energy acquired during continuous stirring. During the aging process, condensation continued to complete the formation of the gel. The spherical molecules started to change their form to flower-like structures as confirmed by the HRSEM and HRTEM images.

3.5. Optical properties analysis

The reflectance spectra of SnO_2, ZnO and SnO_2–ZnO nanocomposites with distinct ratios of SnO_2 to ZnO are shown in Fig. 12. SnO_2, ZnO, 1:1.5 SnO_2–ZnO and 1:2 SnO_2–ZnO show high reflectance at 80 and 90 %; while 1:1 SnO_2–ZnO shows relatively low reflectance around 60 %. SnO_2 is absorbing in the UV region at around ~275 nm [12]. ZnO absorbs at the same regions as the nanocomposites at ~375 nm. Minor peaks in the visible region appearing in all the spectra at 480–500 nm are attributed to instrumental artifacts.

The optical band gaps were estimated from the absorption edges using the Tauc plots presented in Fig. 13. The Tauc relationship used to estimate the band gap energies is given by:

$$\alpha(h\nu) = A\left(h\nu\text{-}E_g\right)^n \quad (3)$$

where A is a proportionality constant, $h\nu$ is the energy of the incident photon, E_g is the band gap, α is the frequency-dependent absorption coefficient and n is equal to 0.5 since the optical transition of SnO_2 and ZnO is a direct band gap.

Extrapolating the sharply rising portions of the curves to the

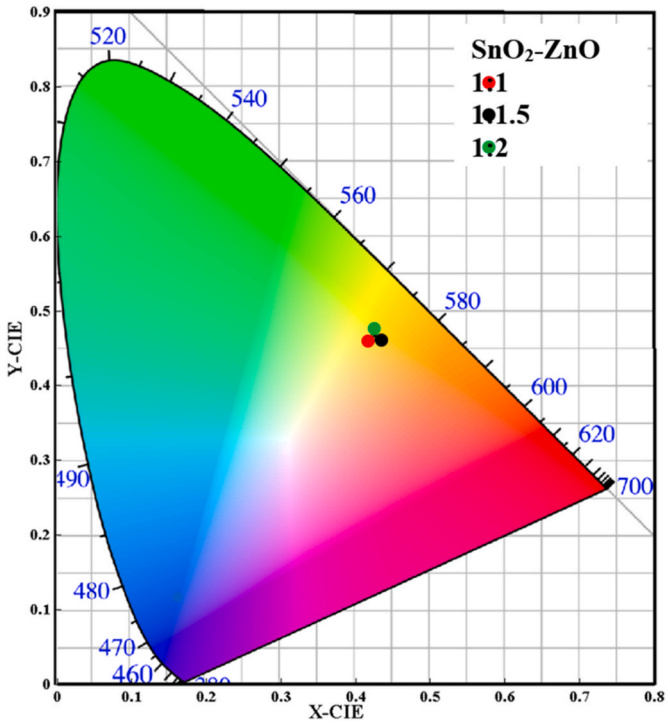


Fig. 17. CIE diagram for distinct molar ratios of SnO_2:ZnO in the nanocomposites.

horizontal axis gave the values of the band gap energies. The band gap energies of SnO_2 (3.80 eV) and ZnO (3.40 eV) are larger than their actual bulk band gaps of 3.6 eV (SnO_2) and 3.37 eV (ZnO). This increase is attributed to quantum confinement effect [25]. The XRD data confirmed that the bandgap increases with decreasing particle sizes. The band gap values of the composite with different ratios of SnO_2 to ZnO were found to be 3.27 (1:1), 3.30 (1:1.5) and 3.32 eV (1:2). The band gap energies increased with increasing Sn:Zn molar ratio. These values are just about that of literature value (3.37 eV) of ZnO.

3.6. Photoluminescence analysis

Fig. 14(a) shows green photoluminescence (PL) broad emission spectrum of the SnO_2 core with a maximum at 562 nm ($\lambda_{excitation} = 325$ nm). This emission is associated with radiative electronic transitions between defect levels within the bandgap. Oxygen vacancies are major defects that act as donor levels for these radiative transitions. This peak was deconvoluted into five peaks, located at 457, 517, 557, 625 and 674 nm using Gaussian deconvolution process. These emission bands are attributed to radiative transition from oxygen vacancies to photoexcited holes in the valence band [13].

The PL emission spectrum of ZnO is shown in Fig. 14(b). The spectrum has two well-known emission bands; one is the UV emission at 380 nm associated with free excitonic recombination [26] and another in the visible emission region at 585 nm ($\lambda_{excitation} = 325$ nm) which is associated with intraband defect states recombination. Also, there is a hump at 750 nm which is not an emission band but an instrumental artefact. The visible yellow emission with a maximum at 585 nm was deconvoluted into two Gaussian peaks located at 572 nm (yellow emission) and 675 nm (red emission). These emissions are attributed to interband radiative transitions where the orange emission is associated with oxygen vacancies (V_o) and the yellow emission with zinc interstitials (Zn_i) [27].

The deconvoluted PL spectra of the SnO_2–ZnO nanocomposites are presented in Fig. 15(a–c). The original (undeconvoluted) spectra consist of the near UV band emission (380 nm) and defects related visible emission band (595 nm). The visible emission band was resolved into overlapping peaks which are due to a contribution from both SnO_2 and ZnO, while the UV emission is assigned to recombination due to excitons in the bandgap of the ZnO nanoparticles. The PL intensity is associated to the concentration of radiative transitions in the sample. Increasing the Sn:Zn ratio influenced the photoluminescence peak intensity of both the UV and visible emissions. The PL emission for 1:1 and 1:1.5 SnO_2–ZnO is less intense than that of 1:2 SnO_2–ZnO.

The defects that formed different energy levels within the band gap were used to propose the mechanism of PL emission. Fig. 16(a–c) illustrate the PL emission mechanisms of SnO_2, ZnO and SnO_2–ZnO, respectively. The most common defects in SnO_2 (Fig. 16(a)) are oxygen vacancies (V_o). $V_o^{\cdot}$ state has the energy close to the conduction band. This energy state is most likely linked to shared electrons with the neighboring Sn^{4+}. $V_o^{\cdot\cdot}$ denotes the $V_o^{\cdot}$ state combined with a hole. When the bandgap of SnO_2 is smaller than the excitation photon energy, the electron can be excited to the conduction band such that the $V_o^{\cdot}$ state attracts a hole from the valence band and hence formed the $V_o^{\cdot\cdot}$ state [28]. The mechanism of a typical process of the PL emission of ZnO includes electronic transitions from the conduction band to defect levels within the band gap that act as energy acceptors and donors, to the valence band. The recombination of trapped and de-trapped electrons with trapped holes give rise to light emissions. The emission comes from the electronic transitions from shallow donor levels (e.g. zinc (Zn_i)) to shallow acceptor levels, and also from vacancies (e.g. oxygen vacancies (V_o) to the valence band) [29].

Fig. 17 shows the International Commission on Illumination (CIE) diagram for distinct molar ratios of SnO_2 to ZnO in the SnO_2–ZnO nanocomposites. The chromaticity coordinates at (0.450,0.462), (0.457,0.465) and (0.454,0.467) show orange photoluminescence for 1:1, 1:1.5 and 1:2 SnO_2 to ZnO molar ratios, respectively. This orange photoluminescence has many uses in applications such as gas discharge fluorescent lamps, light emitting diodes, fluorescent labels, and dyes.

4. Summary and conclusion

ZnO was successfully coated on SnO_2 nanoparticles by a sol-gel synthesis to form nanocomposite structures. The effect of the ratio of Sn to Zn on the crystalline phase, phase formation, surface defects and optical absorption were investigated. The band gap was engineered by varying the ratio of Zn to Sn, which resulted in the shifting of PL emission peak positions and minor changes in the peak intensities. The photoluminescence spectra of the nanocomposites were like those of the ZnO component with emission in the UV (380 nm) and visible (595 nm) range. The nanocomposites were found to have superior PL intensities to the intensities of the individual components (SnO_2 and ZnO). This was ascribed to separation of charges of recombination of electrons and holes from the pairing of SnO_2 and ZnO. The mechanism of radiative transitions was proposed, and the positions of intrinsic defects both in the nanocomposites and individual components were predicted from the PL data.

Credit author statement

Busisiwe Petunia Mabuea: Writing-original draft, preparation, acquisition and analysis of data, revising the paper critically. **Robin Edward Kroon:** Supervision of the lead author, interpretation of data and editing. **Buyisiwe Mavis Sondezi:** Data interpretation, proof reading and editing. **Odireleng Martin Ntwaeaborwa:** Supervision of the lead author, formal analysis, editing, and final approval of the final version for submission.

Author declarations

The authors declare no conflict of interests.

Declaration of competing interest

The authors declare that they have no known competing financial interests or personal relationships that could have appeared to influence the work reported in this paper.

Data availability

Data will be made available on request.

Acknowledgments

The authors are grateful for the financial support from South African National Nanoscience Postgraduate Teaching & Training Platform.

References

[1] B.S. Ghuman, Nanocomposites-A review, J. Chem. Chem. Sci. 5 (2020) 506–510. https://www.researchgate.net/publication/343263485.
[2] G. Murugadoss, K. Thiruppathi, N. Venkatesh, S. Hazra, A. Mohankumar, G. Thiruppathi, M.R. Kumar, P. Sundararaj, J.R. Rajabathar, P. Sakthivel, Construction of novel quaternary nanocomposite and its synergistic effect towards superior photocatalytic and antibacterial application, J. Environ. Chem. Eng. 10 (2022), 106961. https://doi:10.1016/j.jece.2021.106961.
[3] R.G. Chaudhuri, S. Paria, Core/shell nanoparticles: classes, properties, synthesis mechanisms, characterization, and applications, Chem. Rev. 112 (2012) 2373–2433, https://doi.org/10.1021/cr100449n.
[4] S. Yadav, N. Rani, K. Saini, A review on transition metal oxides based nanocomposites, their synthesis techniques, different morphologies and potential applications, IOP Conf. Ser. Mater. Sci. Eng. 1225 (2022), 012004, https://doi.org/10.1088/1757-899X/1225/1/012004.
[5] S. Bhatia, N. Verma, Photocatalytic activity of ZnO nanoparticles with optimization of defects, Mater. Res. Bull. 95 (2017) 468–476, https://doi.org/10.1016/j.materresbull.2017.08.019.
[6] S. Thambidurai, P. Gowthaman, M. Venkatachalam, S. Suresh, Enhanced bacterial performance of nickel oxide-zinc oxide nanocomposites synthesized by facile chemical co-precipitation method, J. Alloys Compd. 830 (2020), 154642, https://doi.org/10.1016/j.jallcom.2020.154642.
[7] T. Jan, S. Azmat, Q. Mansoor, H. Waqas, M. Adil, S. Ilyas, Superior antibacterial activity of ZnO-CuO nanocomposite synthesized by a chemical Co-precipitation approach, Microb. Phatog. 134 (2019), 103579. https://doi:10.1016/j.micpath.2019.103579.
[8] G. Murugadossa, M.R. Kumar, Optical and structural characterization of CdS/ZnS and CdS:Cu^{2+}/ZnS core–shell nanoparticles, Luminescence 29 (2014) 663–668, https://doi.org/10.1002/bio.2603.
[9] T. Uddin, E. Hoque, M.C. Bhoumick, Facile one-pot synthesis of heterostructure SnO_2/ZnO photocatalyst for enhanced photocatalytic degradation of organic dye, RCS Adv 10 (2020), 23554, https://doi.org/10.1039/D0RA03233F.
[10] M. Xu, X. Ruan, J. Yan, Synthesis, Growth mechanism, and photoluminescence property of hierarchical SnO_2 nanoflower-rod arrays: an experimental and first principles study, J. Mater. Sci. B. 51 (2016) 9613–9624. https://10.1007/s10853-016-0169-0.
[11] V. Kumar, H.C. Swart, O.M. Ntwaeaborwa, R.E. Kroon, J.J. Terblans, S.K.K. Shaat, A. Yousif, M.M. Duvenhage, Origin of the red emission in zinc oxide nanophosphors, J. Mat. lett. 101 (2013) 57–60. https://doi:10.1016/J.MATLET.2013.03.073.
[12] A. Kołodziejczak-Radzimska, T. Jesionowski, Zinc oxide-from synthesis to application: a review, Materials 7 (2014) 2833–2881, https://doi.org/10.3390/ma7042833.
[13] I. Musa, S.T. Mahmoud, Synthesis and length dependent photoluminescence property of zinc oxide nanorods, Results Phys. 7 (2017) 3552–3556, https://doi.org/10.1016/j.rinp.2017.09.035.
[14] K. Bouras, J.L. Rehspringer, S. Rinnert, Optical and structural properties of Nd doped SnO_2 powder fabricated by the sol–gel method, J. Mater. Chem. C 2 (2014) 8235, https://doi.org/10.1039/C4TC01202J.
[15] G. Manibalan, G. Murugadoss, S. Hazra, R. Marimuthu, C. Manikandan, R. J Ramalingan, M.R. Kumar, A facile synthesis of Sn-doped CeO_2 nanoparticles: high performance electrochemical nitrite sensing application, J.Inoche. 135 (2021), 109096, https://doi.org/10.1016/j.inoche.2021.109096.
[16] L.C. Nehru, V. Swaminathan, C. Sanjeeviraja, Photoluminescence studies on nanocrystalline tin oxide powder for optoelectronic devices, Am. J. Mater. Sci. 2 (2012) 6–10. https://doi:10.5923/j.materials.20120202.02.
[17] A. Kar, S. Kundu, A. Patra, Surface defect-related luminescence properties of SnO_2 nanorods and nanoparticles, J. Phys. Chem. C 115 (2010) 118–124, https://doi.org/10.1021/jp110313b.
[18] G. Murugadoss, J. Prakash, M.R. Kumar, A.A. Alothman, M.A. Habila, S.G. Peera, Catalysts 12 (2022) 1128, https://doi.org/10.3390/catal12101128.
[19] B.R. Rehani, P.B. Joshi, Crystallite size estimation of elemental and composite silver nano-powders using XRD principles, Indian J. Pure Appl. Phys. 44 (2006) 157–161. https://nopr.niscpr.res.in/handle/123456789/8253.
[20] A. Ayeshamariam, S. Ramalingam, Preparation and characterizations of SnO_2 nanopowder and spectroscopic (FT-IR, FT-Raman, UV–Visible and NMR) analysis using HF and DFT calculations, Spectrochim. Acta A. Mol. Biomol. Spectrosc. 118 (2014) 1135–1143, https://doi.org/10.1016/j.saa.2013.09.030.
[21] P.S. Shewale, K.U. Sim, Y. Kim, J.H. Kim, A.V. Moholkar, M.D. Uplane, Preparation of fluorine-doped tin oxide films at low substrate temperature by an advanced spray pyrolysis technique, and their characterization, J. Lumin. 139 (2013) 113–118. https://doi:10.1088/0268-1242/25/11/115008.
[22] A. Hamrouni, N. Moussaa, F. Parrino, A. Di Paola, A. Houas, L. Palmisano, J. Mol. Catal. Chem. 390 (2014) 133–141. https://doi:10.1016/j.molcata.2014.03.018.
[23] S.U. Ilyas, R. Pendyala, N. Marneni, Dispersion behaviour and agglomeration effects of zinc oxide nanoparticles in ethanol–water mixtures, Mater. Res. Innovat. 8 (2014) 179–183, https://doi.org/10.1179/1432891714Z.000000000953.
[24] H. Mohamed, S. Afridi, A.T. Khalil, D. Zia, Z.K. Shinwari, M.S. Dhlamini, M. Maaza, Phyto-fabricated Cr_2O_3 nanoparticle for multifunctional biomedical applications, J. Inorg. Organomet. Polym. Mater. 30 (2020) 1–14, https://doi.org/10.2217/nnm-2020-0129.
[25] K.F. Lin, H.M. Cheng, H.C. Hsu, W.F. Hsieh, Band gap engineering and spatial confinement of optical phonon in ZnO quantum dots, Appl. Phys. Lett. 88 (2006), 263117, https://doi.org/10.1063/1.2218775.
[26] S.M. Soosen, B. Lekshmi, K.C. George, Optical Properties of ZnO Nanoparticles, SB. 1 and 2 SB, Academic Rev. XVI, 2009, pp. 57–65. https://www.researchgate.net/publication/284063957_Optical_properties_of_ZnO_nanoparticles_prepared_by_chemical_method_using_poly_vinylalcohol_PVA_as_capping_agent.
[27] A.B. Djurisic, C.H. Choy, Photoluminescence and electron paramagnetic resonance of ZnO tetrapod structures, Adv. Funct. Mater. 14 (2004) 856–864, https://doi.org/10.1002/adfm.200305082.
[28] M. Xu, X. Ruan, J. Yan, Synthesis, Growth mechanism, and photoluminescence property of hierarchical SnO_2 nanoflower-rod arrays: an experimental and first principles study, J. Mater. Sci. B. 51 (2016) 9613–9624, https://doi.org/10.1007/s10853-016-0169-0.
[29] T.K. Kundu, N. Karak, P. Barik, Optical properties of ZnO nanoparticles prepared by chemical method using poly (vinylalcohol) (PVA) as capping agent, Int. J. Soft Comput. Eng. 1 (2011) 2231–2307.